Materials & Design 222 (2022) 111075

Contents lists available at ScienceDirect

Materials & Design

journal homepage: www.elsevier.com/locate/matdes

Custom-designed heat treatment simultaneously resolves multiple challenges facing 3D-printed single-crystal superalloys

Sicong Lin [a], Kai Chen [a,*], Weifeng He [b], Nobumichi Tamura [c], En Ma [a]

[a] *State Key Laboratory for Mechanical Behavior of Materials, Xi'an Jiaotong University, Xi'an, Shaanxi 710049, PR China*
[b] *State Key Laboratory for Manufacturing Systems Engineering, Xi'an Jiaotong University, Xi'an, Shaanxi 710049, PR China*
[c] *Advanced Light Source, Lawrence Berkeley National Laboratory, Berkeley, CA 94720, USA*

HIGHLIGHTS

- 3D-printed Ni-superalloy single crystals face four major challenges (***R. A.S.H.)***.
- Designed a single-step treatment to meet all the ***RASH*** requirements.
- Recovery to avoid recrystallization while preventing stray grain growth.
- Optimized annealing duration homogenizes chemical and precipitates distribution.

GRAPHICAL ABSTRACT

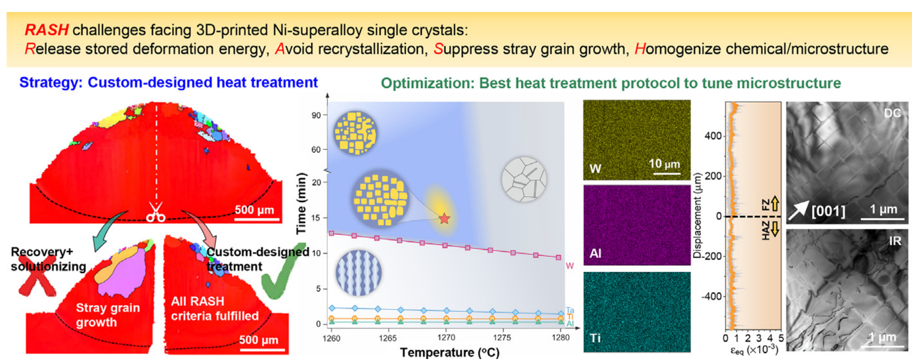

ARTICLE INFO

Article history:
Received 30 June 2022
Revised 14 August 2022
Accepted 17 August 2022
Available online 19 August 2022

Keywords:
Ni-based superalloy single crystals
Heat treatment
Recovery
Recrystallization
Stray grain growth
Chemical homogenization

ABSTRACT

Single-crystal Ni-based superalloys are currently the material of choice for turbine blade applications, especially with the emerging additive manufacturing (AM) that facilitates the manufacture/repair of these single crystals. This promising AM route, however, comes with a dilemma: in the fusion and heat affected zones after e-beam or laser induced melting, one needs a solutionizing annealing to relieve the residual stresses and homogenize the chemical/microstructure. The super-solvus solutionizing temperature is usually adopted from the protocol for the cast superalloys, which almost always causes recrystallization and stray grain growth, resulting in a polycrystalline microstructure and degrading the high-temperature mechanical performance. Here we demonstrate a custom-designed post-printing heat treatment to replace the conventional super-solvus one. The recovery and relatively low temperature diminish the driving force for recrystallization and the movement of stray grain boundaries, without suffocating the chemical/microstructural homogenization thanks to the narrow dendrite width and short element segregation distance. The optimal duration of the heat treatment is proposed to achieve atomic-diffusion mediated chemical homogenization while limiting γ'-particle coarsening in the interdendritic regions. Our strategy makes it practically feasible to resolve several bottleneck problems with one processing/treatment, removing a seemingly formidable obstacle to effective additive manufacturing of superalloy single crystal products.

* Corresponding author.
E-mail addresses: kchenklbl@gmail.com (K. Chen), maen@xjtu.edu.cn (E. Ma).

https://doi.org/10.1016/j.matdes.2022.111075
0264-1275/© 2022 The Authors. Published by Elsevier Ltd.

1. Introduction

Ni-based superalloy single crystals are now widely used for turbine blades and vanes in modern aerospace industries [1]. However, making complicated shapes and internal cooling passages [2] in these single crystals has turned out to be much more difficult and expensive, when compared with conventional precision investment casting [3]. In recent years, 3D printing, also known as additive manufacturing, has emerged as a powerful solution to this problem, not only shortening the processing chain and minimizing the waste, but also providing the possibility to repair damaged and/or worn single crystal superalloy parts to extend their service life [4,5]. Rejuvenation (restoration/repair) of microstructures is effective in extending the life of superalloy blades [6], whereas 3D-printing enables precise shape control. However, while crack free superalloy single crystals have been successfully printed [7–9], their microstructure often fails to meet the homogeneity [10] and stability [11] requirements. In many cases the heat treatment protocol applied to 3D-printed parts is almost the one used for cast parts, with no modification or just shortening of the homogenization time [12]. Nevertheless, as reported previously, due to the inadequate consideration in optimization of heat treatment protocol the nucleation of recrystallized grain across the fusion zone cannot be suppressed [13]. As a result, it is always necessary to devise a suitable post-printing heat treatment, under either ambient or high-pressure conditions [14,15].

To achieve excellent high-temperature performance, Ni-based superalloys incorporate tens of alloying elements, including refractory elements like Re, W and Mo, to form $Ni_3(Al,Ti)$ γ'-precipitates with $L1_2$ structure that are coherent with the solid-solution-strengthened austenitic γ-matrix [16,17]. When produced with the 3D printing approach, the superalloy is deposited layer-by-layer through local melting of the powder feedstock with designed chemical constituents using either a laser or an electron beam heat source [18–20]. Superalloy single crystals are produced under a steep temperature gradient [21], which outperform their polycrystalline counterparts in terms of resistance to creep and fatigue [7,11]. Another advantage brought by the high cooling rate is the relatively fine dendrite structure (several micrometers in width [22]) and consequently suppressed chemical inhomogeneity across dendrites compared to cast superalloys in which the dendrites are usually hundreds of microns wide [23]. Stray grains tend to form on metal surface where the temperature gradient is no longer parallel to the building direction [24,25], thus they are inevitable in 3D-printed superalloy single crystals on both the outer surface of the blades and the inner surfaces of the internal cooling structures [7]. The outer surface can be machined and/or milled to regain the single crystalline structure, but not the inner surfaces of the cooling structures. Fortunately, the local service temperature near the inner surfaces is lower than that at the outer surface by several hundred degrees Celsius; the stray grains there are bearable as long as they do not grow much larger into the interior [26,27]. During solidification, the γ-matrix forms first, and ejects the γ'-forming elements into the remaining liquid in-between the dendrites, lowering the liquidus temperature [28]. Once the interdendritic liquid solidifies, its solvus temperature is elevated due to enriched γ'-formers, and as a result the γ'-precipitates in these regions form earlier and grow bigger than those in dendrite cores (DCs). Also, the γ'-precipitate volume fraction and mechanical properties become inhomogeneous across the dendrite width [29–32]. Another issue arising from the rapid cooling rate is the high thermal stress [33–35]. The high-density dislocations induced by thermal stress provides the driving force for recrystallization in the bulk, and for stray grain boundary migration near the surface, both of which are detrimental or even disastrous, as they ruin the single-crystalline microstructure desired for retaining high-temperature mechanical properties.

From the discussion above, there appear to be four major challenges facing the post-printing heat treatment for 3D-printed superalloy single crystals. Specifically, a successfully customized protocol must be able to (1) ***r***elease most of the stored energy due to dislocation defects (excess enthalpy, stored in the crystal lattice, associated with the dislocations generated by the internal stress) [10], (2) ***a***void recrystallization completely [7,11,36], (3) ***s***uppress stray grain growth as much as possible [25,37], and (4) ***h***omogenize the chemical/microstructure distribution to a level comparable with that in cast alloys [12]. From here on these requirements are acronymized as the ***RASH*** challenges. In this paper, we evaluate previously reported heat treatment protocols against these four demands, and then design a novel and yet simple heat treatment, which will be demonstrated to accomplish all the ***RASH*** actions via a solutionizing annealing prior to aging treatment.

This new strategy is conceived based on the following two considerations. First, since the diffusion distance, which is proportional to dendrite width, is greatly reduced in the 3D-printed superalloy due to the fast cooling rate, chemical homogenization at a level similar to the super-solvus solutionizing treatment in the traditional cast products can be achievable with a treatment at a temperature between the solvus point of the DCs and that of the interdendritic regions (IRs); this temperature is lower than the conventional solutionizing annealing temperature for superalloy single crystals, which is above the solvus temperature, usually conducted at 1300 °C or higher, to dissolve all the precipitates across DCs and IRs completely. In our new case, undissolved precipitates remain. Second, by setting the solutionizing temperature above the solvus of the γ'-precipitates in the DCs while below that in IRs, the dislocations moving freely in the DCs allow for a speedy recovery. In the meantime, the undissolved γ'-precipitates in IRs would be able to impede the massive motions and interactions of dislocations, nucleation of recrystallized grains, and migration of stray grain boundaries [6]. The success of such a novel treatment will be demonstrated in the following, in three types of superalloy single crystals with different chemical constituents produced using either a laser or an electron beam heat source.

2. Material and methods

In this study, three types of superalloy single crystals were investigated, which were electron beam melted AM3, laser directed energy deposition 3D-printed AM3, and laser directed energy deposition 3D-printed SRR99. The nominal compositions of AM3 and SRR99 and their alloyed powders used here are Ni-8Cr-5.5Co-2.25Mo-5W-6Al-2Ti-3.5Ta and Ni-8Cr-5Co-10W-5.5Al-2.2Ti-3.0Ta in weight percentage, respectively. The [001] cast AM3/SRR99 single crystal base-metal boules were cut into cylinders ~ 4 mm in height. Electron beam melting with no feedstock was carried out using a DMAMS Zcomplex3™ electron-beam 3D-printing system operated in a 10^{-3} mbar vacuum. Electron beam of 15 mA was accelerated to 60 keV and focused onto the base metal surface to form a melt pool. Line scanning was programmed with the velocity of 10 mm/s to ensure epitaxial dendrite growth in the melt pool. A fusion zone (FZ) of about 1500 μm in width and 800 μm in depth was generated. Laser 3D-printing was conducted on an in-house developed coaxial laser cladding apparatus equipped with a CO_2 laser with a beam size of 2 mm. The gas atomized superalloy powders with diameters ranging from 48 to 180 μm with similar composition to the base metal were coaxially injected at a 11 g/min feeding speed by high-purity Ar gas carrier into the molten pool formed by the laser beam with a power of 2000 W and 2 mm/s laser scanning speed. The interlayer spacing was 0.2 mm with a back-and-forth scan path. Therefore, the molten powder solidified on top of the crystal and deposited layer by layer. More detailed information about the manufacturing process can be found elsewhere [38].

Three heat treatment approaches were employed and compared in this study. In our novel heat treatment protocol with solutionizing annealing, the electron beam melted and laser 3D-printed single crystal superalloys were first solutionized at an optimized temperature and then aged at 1100 °C and 870 °C for 6 h and 20 h, respectively. The optimized solutionizing condition was optimized to be 1270 °C for 15 min. Comparisons were made with identical electron beam melted and laser 3D-printed samples, heat treated via two other protocols. The "standard heat treatment" was carried out in a similar manner as the novel heat treatment, except that the solutionizing treatment was at 1300 °C. Note that the duration of the so-called standard solutionizing heat treatment was significantly shorter than that in the superalloy handbook, because of the narrow dendrite width. The last heat treatment process involves a recovery annealing step at 1100 °C for 6 h, prior to the standard heat treatment. The heating rate of all specimens was set at 15 °C/min. All the heat treatment experiments were performed using a CARBOLITE® RHF 1500 muffle furnace, equipped with an R-type thermocouple installed at the center of the back inside wall of the furnace chamber to monitor the temperature. In order to verify the accuracy of the temperature, an AM3 cast superalloy single crystal was firstly solutionized at 1300 °C for 3 h and then annealed at temperatures from 1260 to 1280 °C for 30 min, respectively. The solvus temperature of the γ'-precipitates in the DCs was measured to be between 1260 °C and 1270 °C and between 1270 °C and 1280 °C in the IRs, respectively, through secondary electron images taken with a SEM (Fig. S1), which is in agreement with the literature [39]. All samples were air cooled at the rate of approximately 300 °C/min once the heat treatment was finished.

The microstructure was examined under secondary electron mode in a SEM after etching in 25 % phosphoric acid water solution at the voltage of 5 V for 10 s. WDS for element distribution study was conducted in a SuperProbe JXA-8230 Electron Probe Microanalyzer at the accelerating voltage of 20 kV. EBSD was carried out after the sample surface was polished electrochemically in 10 % perchloric acid alcohol solution at the voltage of $\sim$ 30 V for 60 s. All TEM images displayed in this manuscript were taken in a JEM-2100F field emission electron microscope at the accelerating voltage of 200 kV. X-ray microdiffraction (μXRD) sample was electro-polished in the same way, and then scanned using micro-focused synchrotron polychromatic X-ray beam on Beamline 12.3.2 at the Advanced Light Source of Lawrence Berkeley National Laboratory [40]. The collected Laue diffraction data were processed using a custom-developed software based on the peak position comparison method to measure [41,42] and visualize [43] the strain distribution accurately. Diffraction peaks were searched based on a user-defined peak to background threshold and fitted using a 2D Lorentzian function to obtain the peak position precisely. By comparing the angles between experimentally measured diffraction peak positions with the theoretically calculated ones, the strain tensor and thus the equivalent strain are calculated. TEM specimens were prepared using the conventional twin-jet electropolishing.

3. Results

3.1. Necessity for custom-designed heat treatment

As illustrated in the upper panel of Fig. 1a, the standard heat treatment of cast superalloys consists of hours of super-solvus solutionizing treatment to homogenize the chemical distribution, followed by a long period of aging treatment to precipitate out, ripen and stabilize the γ'-precipitates [37,39,44]. However, with such a heat treatment, recrystallization sets in readily from the heat affected zone (HAZ), and the newly formed recrystallization grains as well as the existing stray grains grow large quickly as the grain boundary mobility is high once the specimen is heated above the solvus temperature (Fig. 1b). This recrystallization, rendering the single crystal polycrystalline, wastes all the efforts that have been made to achieve the single-crystalline microstructure desired for high temperature mechanical properties. Clearly, the standard heat treatment cannot meet the ***RASH*** challenges for 3D-printed superalloy single crystals.

Efforts have been made before, to solve the recrystallization issue by applying a pre-solutionizing annealing step to the 3D-printed superalloy single crystals at sub-solvus temperature, as shown in the middle panel of Fig. 1a. With this step, a large fraction of the stored energy due to dislocation defects is released prior to solutionizing treatment, taking away the driving force for recrystallization [10]. Afterwards, the standard ageing process is employed, which produces cuboidal γ'-precipitation microstructure indistinguishable from the cast base metal. However, stray grain growth is not precluded during the super-solvus solutionizing treatment, because the migration of high-angle grain boundaries is activated, as indicated by the crystal orientation distribution (inverse pole figure) maps obtained from electron backscatter diffraction (EBSD) scans before and after (Fig. 1c) heat treatment of a laser 3D-printed single-crystalline superalloy AM3 specimen. Similar observations have also been recorded in electron beam melted superalloy single crystals (Fig. 2). This necessitates a surface subtractive machining process before super-solvus solutionizing heat treatment, to get rid of the seeds of stray grains. Such an extra machining step is not feasible for internal cooling structures, and is in any case time-consuming and costly.

Considering that both recrystallization and stray grain growth occur under the precondition of the complete solid-solutioning of γ'-precipitates, we have conceived a different heat treatment protocol. It also consists of two steps of solutionizing and aging treatment, but the solutionizing treatment is carried out at lower temperature (1270 °C for 30 min in this case) instead of the conventional super-solvus one, as displayed in the bottom panel of Fig. 1a. The specimen is exactly the same as the one used for recovery pre-annealing plus super-solvus solutionizing heat treatment, but a pronounced difference in stray grain size is seen in Fig. 1d in laser 3D-printed superalloy single crystal AM3. As shown in Fig. 2, when the additive manufacturing heat source is changed to electron beam, this method still works well, although here no feedstock is supplied. In other words, combining recovery annealing and super-solvus solutionizing into a solutionizing heat treatment at a temperature between the solvus point of the DCs and that of the IRs meets the "avoid recrystallization" and "suppress stray grain growth" requirements. In the next section, we will further tune the temperature and duration of this custom-designed heat treatment to homogenize the chemical and microstructure distribution.

3.2. Optimization of annealing temperature and duration

In order to meet all the ***RASH*** requirements, the annealing temperature and duration need to be carefully tailored and optimized. Firstly, the microstructure and residual strains of the as-electron-beam-printed superalloy single crystal are demonstrated in Fig. 3. The γ'-particles are tiny (30–50 nm in diameter) and irregular in the DCs, whereas in the IRs they appear in almost cuboidal shape with rounded corners and edge length of 70–100 nm. Based on the contrasted size and shape distribution, the dendrite widths

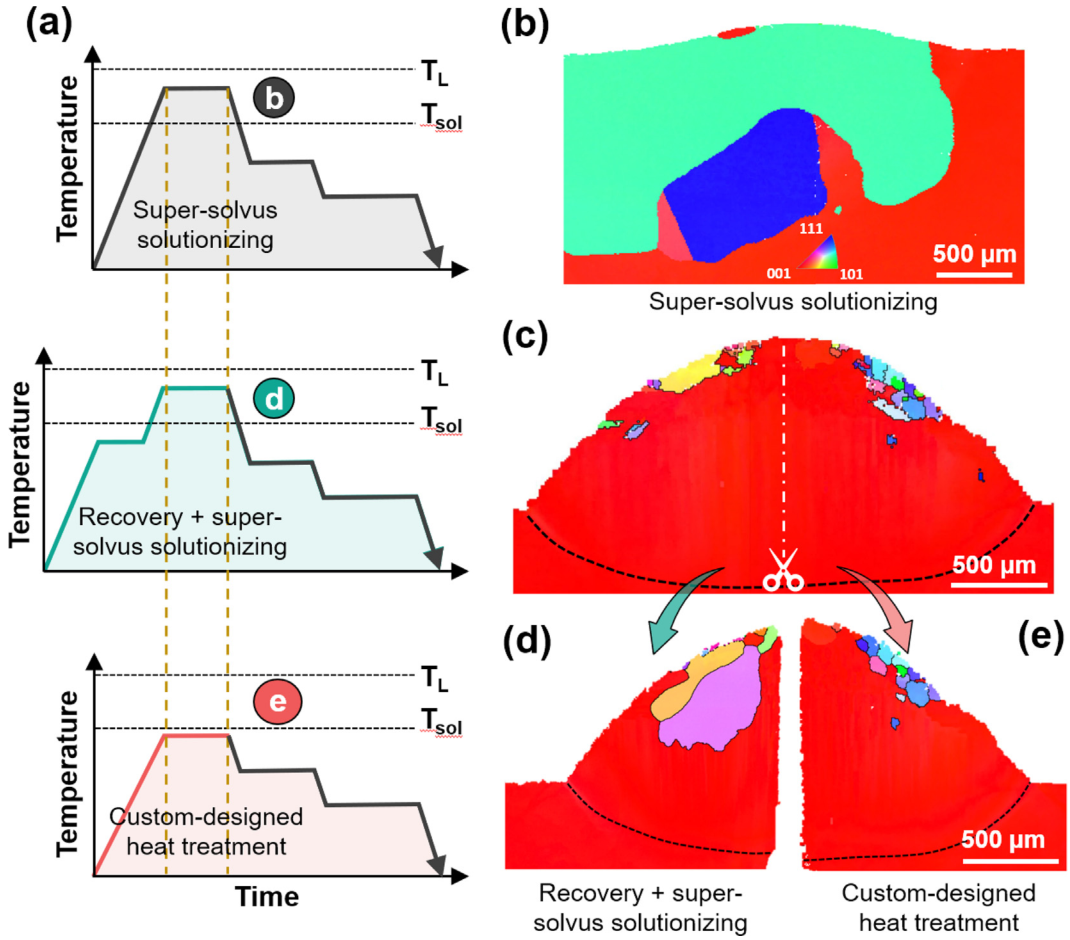

Fig. 1. Crystal orientation distributions resulted from various heat treatment protocols. (a) Three different heat treatment protocols are considered. (b) Direct super-solvus treatment results in recrystallized microstructure. (c) As-printed single crystal superalloy. (d) Recovery (pre-annealing) before super-solvus treatment helps to prevent recrystallization, but stray grains grow bigger. (e) Custom-designed heat treatment at 1270 °C eliminates both recrystallization and stray grain growth. T_L and T_{sol} in (a) stand for liquidus and solvus temperatures, respectively. (b - e) are the inverse pole figures obtained from EBSD mapping scanned with 10 μm, 3 μm, and 3 μm step size, respectively. (c - e) show a quasi-in-situ experimental results of the almost identical area before and after heat treatment.

are measured to span from 3 to 10 μm in FZ. Micro-segregation is clearly seen from the X-ray wavelength dispersive spectra (WDS) maps, showing enriched W in DCs, and Ti and Al in IRs. After electron beam melting, the crystal is riddled with dislocations [45]. The elastic strain associated with these defects is measured using synchrotron-based μXRD. An area of 80 μm (horizontal) × 1150 μm (vertical) across the FZ and the heat affected zone (HAZ) is scanned using a micro-focused polychromatic X-ray beam with 2 μm spatial resolution, as marked in Fig. S2, and the lattice strain tensor at each scanning position is measured from the Laue diffraction pattern. The equivalent strain ε_{eq} is calculated from the strain tensor, as a representative of the magnitude of the local strain, $\varepsilon_{eq} = \frac{\sqrt{2}}{3}\sqrt{(\varepsilon_{xx}-\varepsilon_{yy})^2 + (\varepsilon_{yy}-\varepsilon_{zz})^2 + (\varepsilon_{zz}-\varepsilon_{xx})^2 + 6(\varepsilon_{xy}^2+\varepsilon_{xz}^2+\varepsilon_{yz}^2)}$, where ε_{ij} is one of the six strain tensor components. As shown in Fig. 3c, the equivalent strain varies pronouncedly in the building direction, but is quite uniform in the horizontal direction; in Fig. 3d the average equivalent strain magnitude is therefore plotted as a function of the distance to the melting line. The highest lattice strain, ~4×10^{-3}, appears near the interface between FZ and HAZ. It decreases gradually into FZ, reaches the minimum value of 1.5×10^{-3} at the position about 350 μm away from the interface, and increases slightly to an almost steady 2×10^{-3}. In the HAZ, the strain distribution is even more non-uniform. The equivalent strain drops to almost zero in a range of 300 μm and then increases back to $\sim 3 \times 10^{-3}$. Although the exact elastic stiffness tensor for AM3 single crystal was not obtained, the peak tensile residual stress is estimated (assuming a modulus of the order ~ 200 GPa) to be on the order of 0.8 GPa. This stress is rather high and likely to cause local deformation with dislocation accumulation, providing a fertile site for recrystallization nucleation when the temperature is elevated to 1300 °C, at which the migration of high-angle boundaries is potent, Fig. 1b. The dislocation density and structure, which is strongly influenced by not only the stress but also the γ/γ' structure, are studied under a transmission electron microscope (TEM). As seen in the bright-field image in Fig. 3e, curly dislocations near the melting line, where only tiny γ'-particles exist, are heavily tangled, with a density of approximately 6×10^{14} m^{-2} measured using the line-intercept method [46]. In the HAZ, the density of dislocations is similar to the interfacial area, while the structure is quite different. Because the primary γ'-particles are only partially dissolved, γ-channels are narrower and dislocations are straight and parallel, with pile-ups at the γ/γ' interfaces [47].

Secondly, the solvi of the γ'-precipitates in DCs (T_1) and IRs (T_2) are measured by annealing the specimen at various temperatures for a constant period of time (15 min in this study) and then monitoring the evolution of the SEM image contrast. Once the electron-beam-printed AM3 superalloy was annealed above T_1 (1260 °C, as displayed in Fig. 5a), the γ'-precipitates in the DCs are fully dissolved and then reprecipitate as larger and almost uniform

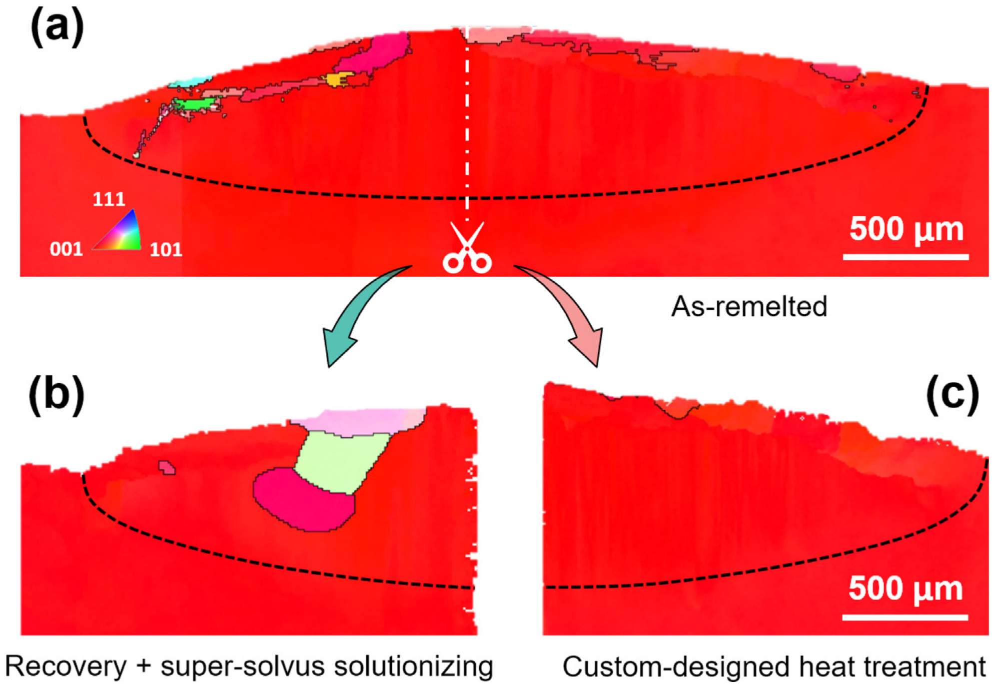

Fig. 2. The crystal orientation map of the electron-beam-melted AM3 superalloy single crystal showing the same area from a quasi-in-situ experiment: (a) as-melted, (b) after recovery and super-solvus solutionizing, and (c) after the novel heat treatment. The stray grain seeds on the top surface grow much bigger during super-solvus heat treatment but stay almost unchanged after the novel heat treatment.

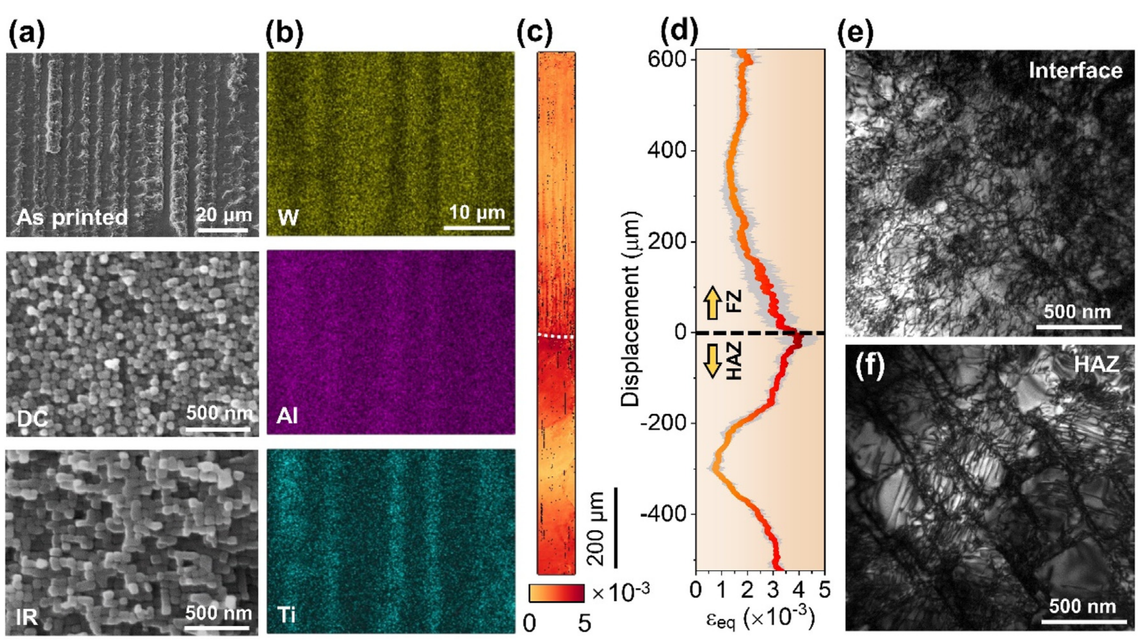

Fig. 3. Microstructure of the electron-beam-melted AM3 superalloy single crystal. Distributions of (a) γ' particles, (b) constituent elemental species, (c-d) equivalent strain, and (e-f) dislocation structures are all inhomogeneous.

cuboids; meanwhile, the γ'-precipitates in the IRs are partially dissolved, resulting in the disappearance of the contrast between DC and IR in some regions. As the annealing temperature goes above T_2 (1280 °C in this case), the contrast between DC and IR becomes almost homogeneous. These observations suggest that the optimized temperature for the solutionizing heat treatment lies between the solvi from 1260 °C to 1280 °C.

To guide the selection of the duration time, the diffusion equation $d = \sqrt{4Dt}$ is employed [12]. By taking the reported diffusion coefficient D of alloying elements Al, Ti, Ta, and W [48] and setting the diffusion distance d as half of the dendrite width (5 μm), the diffusion time t is calculated for each temperature between 1260 °C and 1280 °C. The pace setter, W, migrates the most slowly and the annealing time needs to be longer than 13 min when the specimen is heat treated at 1260 °C, and 10 min for 1280 °C. For experimental verification of the calculation, the 3D-printed specimen is annealed at 1270 °C for 10 min, ~15 % shorter than the calculated time. The chemical composition distribution is found still inhomogeneous, as seen in the WDS map in Fig. 5b. Therefore, in the following the annealing time of all experiments is no shorter than the calculated values.

The resulting microstructure is sensitive to the annealing temperature. As displayed in Fig. 5c, after annealing at 1276 °C for 10 min, stray grains grow rapidly and overwhelm the whole electron-beam-printed volume. Consequently, the desired annealing temperature should be set below 1276 °C to fulfill the "suppress stray grain growth" and "avoid recrystallization" requirements.

In order to understand how temperature and time influence the homogeneity of the γ' microstructure, identical specimens were solutionizing annealed at 1270 °C for 15 min and 30 min, respectively (Fig. 5d). For the same period of time (15 min), 1270 °C annealing results in the γ' microstructure with less contrast than that annealed at 1260 °C; while extending the annealing time (from 15 min to 30 min, or even longer as shown in Fig. 4) results in more pronounced contrast and thus microstructural inhomogeneity. Same result has also been reported lately on designing heat treatment protocol of laser deposited single crystal superalloy [49]. Overall, using a shorter time at a higher temperature generates a more homogeneous microstructure.

By plotting the observations above into a single "treasure map", we close in on the desired heat treatment protocol, as demonstrated in Fig. 5e. In this map, the boundaries are demarcated by the several considerations outlined in the preceding paragraphs. Specifically, the gray areas in this map are not acceptable, as these conditions would subject the alloy to either recrystallization/stray grain growth (increasing in degree when moving to the right), or inhomogeneous chemical composition (increasingly inhomogeneous moving towards the bottom). Only in the blue region, can recrystallization and stray grain growth be successfully prevented, and the chemical uniformity achieved. The bottom right corner of the blue region, indicated by the yellow zone, is the most favorable, because lower temperature together with longer annealing time would be harmful for the γ' particle size homogeneity [49]. Going in this direction leads us to the best spot (1270 °C for 15 min, as marked by a red star).

3.3. Stress/strain and microstructural characterization

After heat treatment, the γ'-particles in the IRs are about 200–300 nm in edge length, bigger than those in the DCs ($\sim$100 nm). The γ channels in the IRs widens to $\sim$ 30 nm, also wider than those in the DCs (only a few nm). No contrast remains between the DCs and IRs in the WDS maps of the FZ. The element maps of W, Al, and Ti displayed in Fig. 6b indicate little chemical inhomogeneity after the new heat treatment. This is confirmed by the significantly reduced fluctuations in the element distribution line scans across the dendrites when compared with the scans before (Fig. 7, It is noted that the line scans were carried out on identical specimens, but not exactly at the same position). The equivalent strain map in Fig. 6c reveals directly that the lattice strain in the interfacial region, where the strain is high and inhomogeneous in the as-printed state, becomes low and uniform. Detailed analysis shows that the equivalent strain has a nearly constant magnitude at about 0.5×10^{-3}, which is roughly the lower-bound measurement limit of the μXRD technique. The dislocations still show a distribution that is moderately non-uniform, after heat treatment. The DCs become almost dislocation free, with only 2 dislocations in the observed area (Fig. 6e). But in the IRs, the dislocation density is higher (5×10^{13} m^{-2}) and more inhomogeneous, as observed in Fig. 6f. From other TEM images taken in the same specimen, the dislocation density is in a range from 3×10^{13} m^{-2} to 1×10^{14} m^{-2}.

From the results above, we conclude that all the four ***RASH*** challenges are resolved via the custom-designed heat treatment. That is, the stored energy due to dislocation defects is released, recrystallization is avoided, stray grain growth is suppressed, and the chemical distribution is homogenized. What is to be dealt with next, is the morphology of the γ'-particles that subsequently evolve during ageing, and the remaining (left-over) dislocation contents. After the heat treatment at 1270 °C for 15 min, the electron-beam-printed AM3 single crystal is aged following the standard heat treatment protocol to evolve the γ'-particles. In the DCs, regular cuboidal γ'-particles with the side length of 450 nm are obtained in both FZ and HAZ, and recovery reduces the dislocation density (Fig. 8a and b) to less than 1 % of that in the as-printed single crystals, and only individual dislocation can be detected occasionally. However, inside the IRs the microstructure is not fully uniform. In the IRs in FZ, γ'-particles coarsen moderately, and dislocations are observed to align parallel to the γ/γ' phase boundaries (Fig. 8c). The dislocation density in this region is 5×10^{13} m^{-2}, about 10 times lower than that in the as-printed state while 10 times higher than that in the DCs. In the IRs in HAZ, coarsening of γ'-precipitates can be observed. From the bright-field TEM image in Fig. 8d, the γ'-precipitates are embraced by dislocations; this is because the majority of the dislocations trying to recover are blocked effectively by the strengthening precipitates, while only a small proportion of dislocations penetrate into γ'-precipitates. The dislocation density in this region is measured

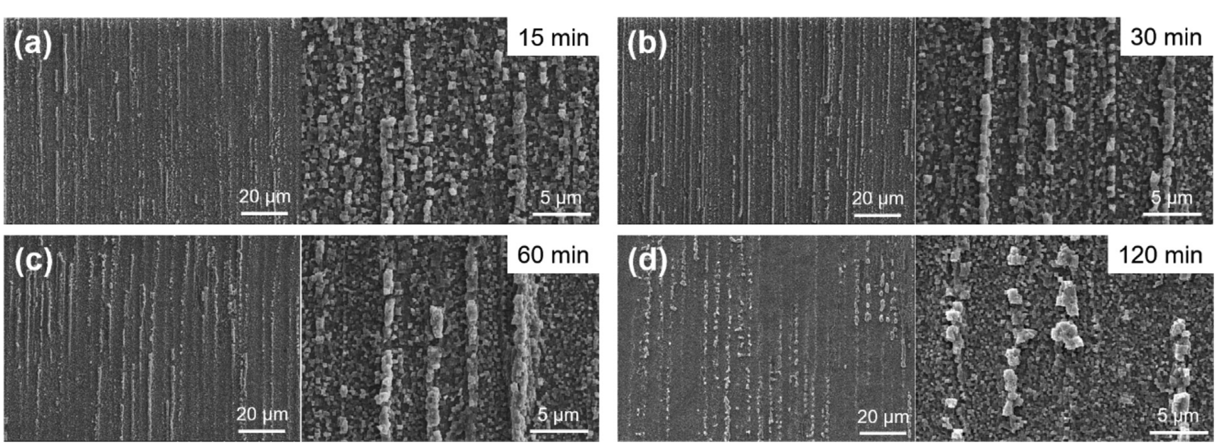

Fig. 4. The microstructure of electron-beam 3D-printed AM3 superalloy single crystal after being solutionizing annealed at 1270 °C for (a) 15 min, (b) 30 min, (c) 60 min, and (d) 120 min. The γ'-precipitates in the IRs were measured $\sim$ 510 nm, 700 nm, 1000 nm, and 1320 nm, respectively, indicating they become more and more coarsened as the duration elongates.

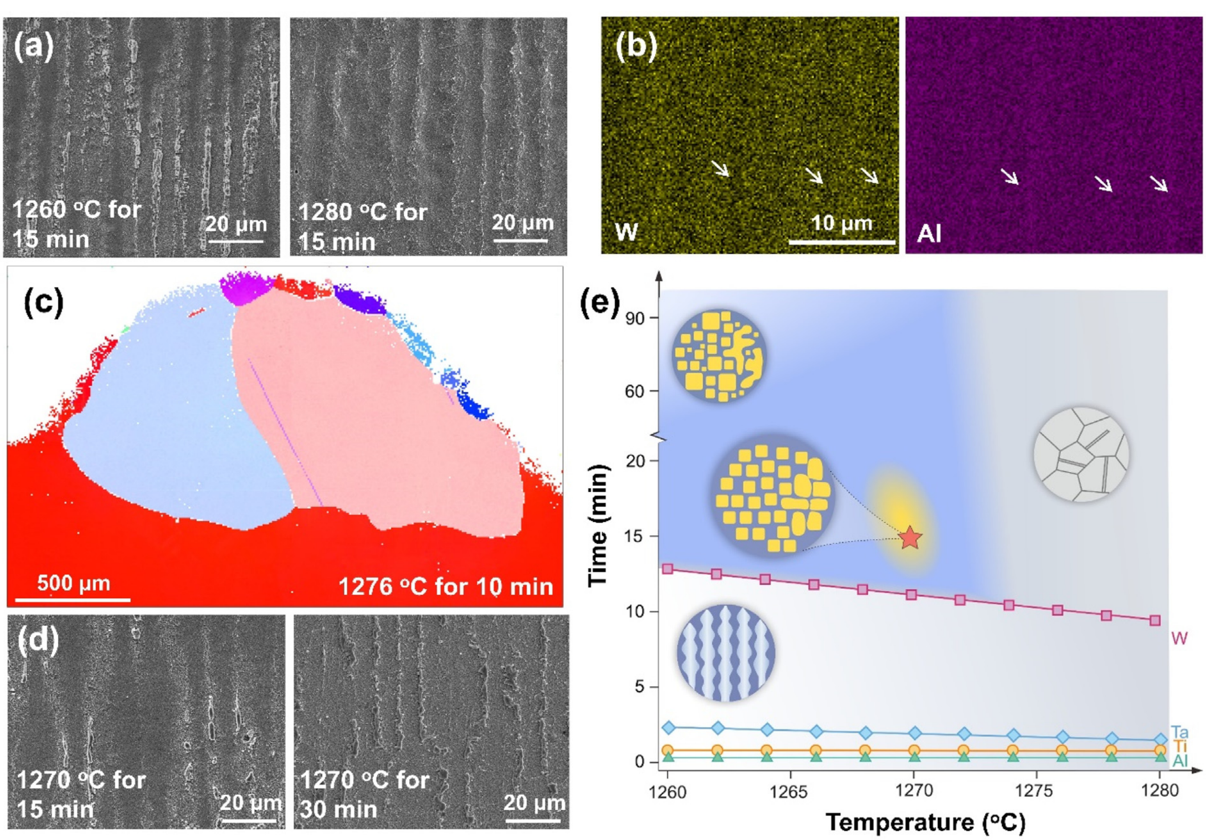

Fig. 5. Optimization of heat treatment temperature and time. (a) The microstructure evolution of the γ′-particles in the electron-beam-printed AM3 superalloy, after annealing at 1260 and 1280 °C for 15 min. (b) shows the chemical inhomogeneity across dendrites when time is insufficient. (c) is the inverse pole figures obtained from EBSD mapping scanned with 10 μm step size. (d) The contrast of γ′-particles becomes weaker after annealing at 1270 °C for 15 min. (e) shows a treasure map locating the optimized heat treatment parameters (yellow region with red star).

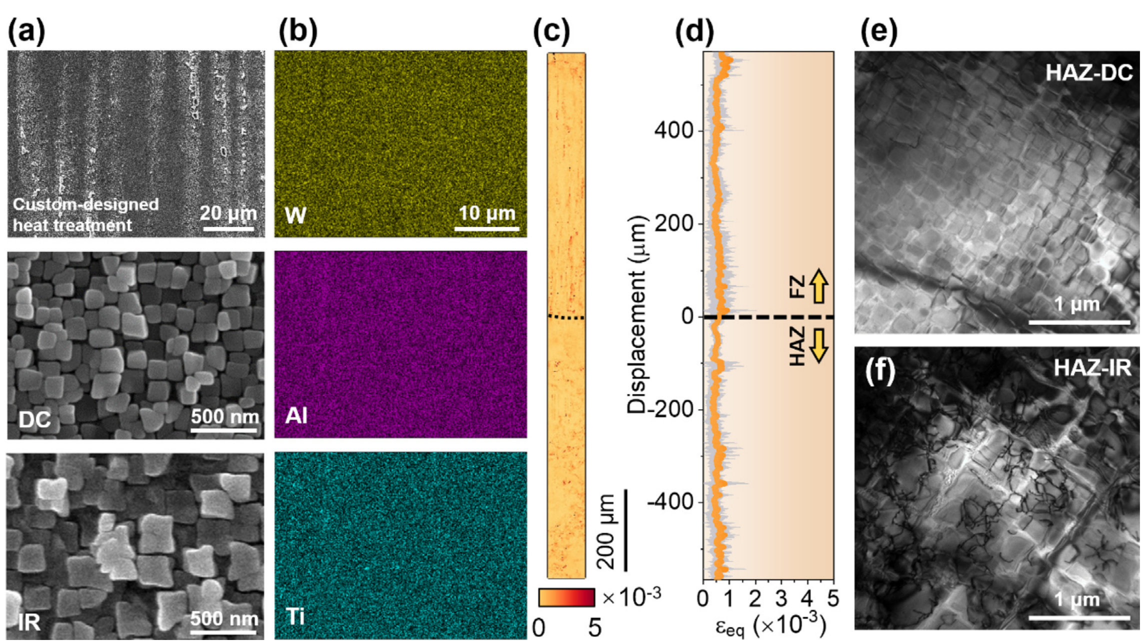

Fig. 6. Microstructure after the heat treatment of the AM3 superalloy single crystal. The distributions of (a) γ′-precipitations, (b) element and (c-d) equivalent strain become homogeneous, although (e-f) dislocation densities in the DC and IR are different.

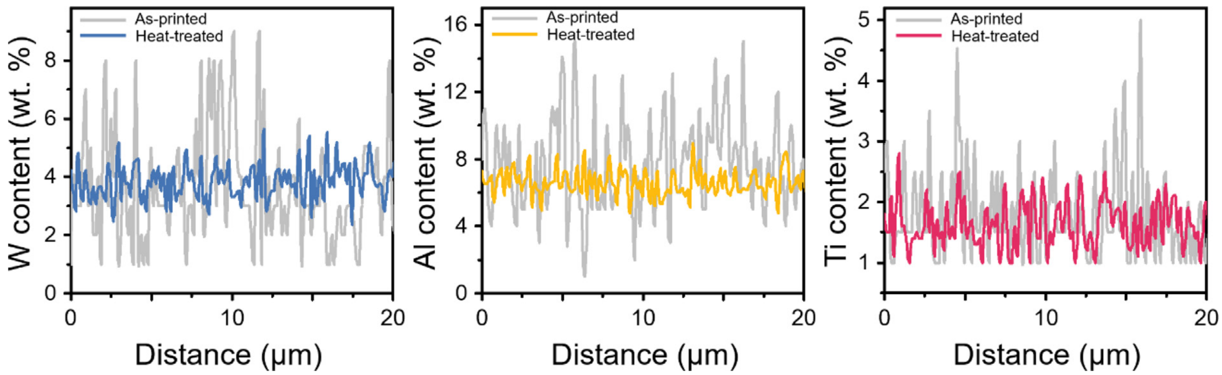

Fig. 7. Element distribution across the dendrite width before and after our new heat treatment.

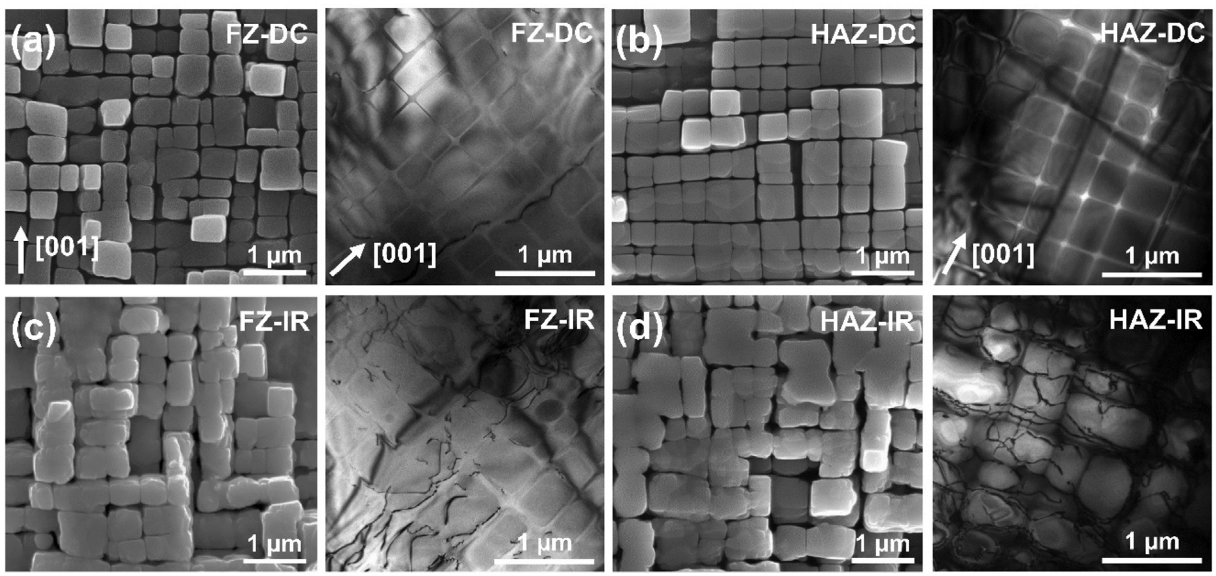

Fig. 8. Microstructure of AM3 superalloy single crystal after heat treatment, 1270 °C for 15 min with subsequent ageing treatment. γ'-precipitates in the DCs of (a) FZ and (b) HAZ are uniform and dislocations are completely annihilated. Coarsening of γ'-precipitates in the IRs of (c) FZ and (d) HAZ occurs and dislocations tend to reside along the γ/γ' interface.

to be approximately 10^{14} m^{-2}, higher than that in the IRs of FZ but still 5 times lower than that in the as-printed single crystals. The microstructure distributions of the γ'-particles of the fully heat treated laser 3D-printed superalloys after heat treatment (Fig. S3) are quite similar to those in the electron beam melted one.

It must be noticed that the size and/or morphology of the γ'-particles in the fully conventionally heat-treated cast superalloys are not completely homogeneous either [50], mainly because the dendrite widths of cast superalloys are on the order of hundreds of microns such that the chemical composition from the DCs to the IRs cannot be homogenized even when the solutionizing heat treatment is carried out above the solvus temperature. Therefore, the minor inhomogeneity resulted from our novel heat treatment is believed to be acceptable. More details about this inhomogeneity will be discussed further in the next section.

4. Discussion

Post 3D-printing heat treatment, as one of the most effective approaches to tune the microstructure and thus mechanical properties of superalloys, has attracted a lot of attention. Because of the fine dendritic structures, shortening the heat treatment time has been proposed; however, the solutionizing temperatures in previous reports are still higher than the solvus of γ'-precipitates, under either ambient or high pressures [12,15]. This is because in many of these previous investigations the 3D-printed superalloys are polycrystalline, and thus recrystallization is acceptable. For 3D-printed single crystals, ***RASH*** issues pose major challenges – low temperature for short time leads to inhomogeneous chemical distribution, while high temperature (higher than 1320 °C for example) for even very short time may still trigger recrystallization. Exploiting the fact that the presence of γ'-particles can impede the motion of dislocations and high-angle grain boundaries, we have designed a novel heat treatment approach to achieve recovery and chemical homogenization with a solutionizing annealing step at a temperature between the solvus point of the DCs and that of the IRs. Different from the previously employed super-solvus solutionizing heat treatment, which just adopts the solutionizing temperature from the standard heat treatment protocol established for the cast superalloys, the solutionizing temperature is optimized in a two-step manner: firstly measuring the solvi of γ'-particles in DCs and IRs, and then further specifying the critical temperature that does not induce recrystallization and stray grain growth.

We now take a closer look at the mechanisms as to how the ***RASH*** issues are resolved. As illustrated in Fig. 9, a high-density

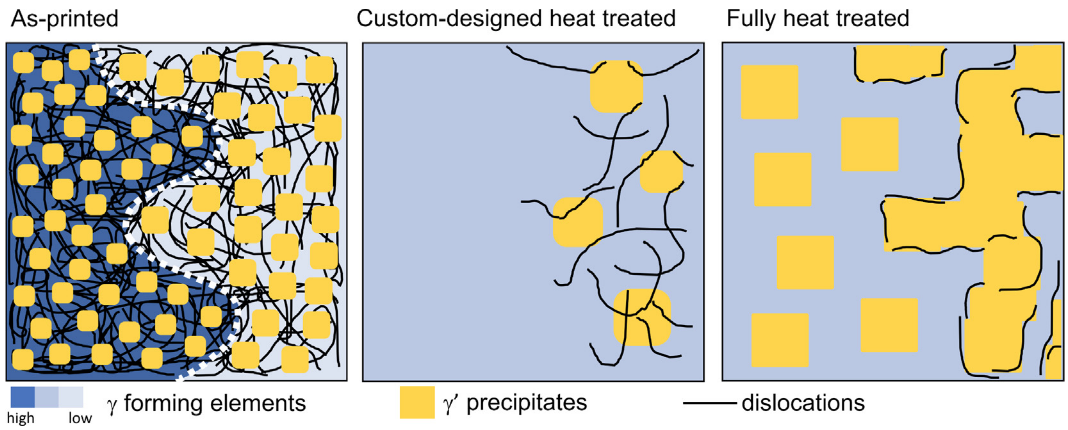

Fig. 9. Evolution of γ'-precipitate size/morphology and dislocation density/configuration during the heat treatment and subsequent aging heat treatment. Light and dark blue colors in the as-printed state indicate chemical inhomogeneity, which is homogenized after heat treatment.

of dislocations, non-uniform chemical composition, and non-identical γ'-particle size/morphology are formed in the as-printed superalloys, although the non-uniformity is the most obvious at locations on the surface. When the temperature is elevated to above the solvus temperature (1280 °C for the AM3 superalloy single crystal in this report) of the DCs but below the IRs, atomic diffusion easily covers half of the dendrite width (only a distance of 10 μm or less in 3D-printed superalloys), to achieve compositional homogeneity. Since the γ'-particles in the DCs are totally dissolved, dislocations move readily without obstacles to mediate recovery. In the IRs, although the much wider γ-channels provide a spatial playground for dislocations to interact with one another, γ'-particles in these regions are not fully dissolved and the remnants impede the motion of dislocations and high-angle grain boundaries. This is why the dislocation density is brought down effectively and meanwhile recrystallization is largely avoided and stray grain growth is suppressed. These left-over dislocations and their associated energy, during the aging heat treatment, provide the driving force for γ'-particle growth, which is similar to the coarsening mechanism discussed previously [51].

An interesting question is whether it is possible, and how, to further enhance the homogeneity. It is obvious that elevating the solutionizing heat treatment temperature would promote the homogeneity of the size and morphology of γ'-precipitates, because recovery would be more thorough, leaving less dislocations and lower residual strain/stress after heat treatment. However, higher solutionizing temperature also increases the likelihood for recrystallization and stray grain growth, especially the latter. As we observed, stray grains grow bigger significantly at 1276 °C after annealing for 10 min (Fig. 5c). Consequently, we conclude that while the compositional homogeneity is relatively easy to achieve, the γ'-morphology homogeneity is counterbalanced by the risk of forming high-angle grain boundaries that are prone to migration. This trade-off could lead to an optimized solutionizing temperature. As for treatment durations, systematic investigation shows that extending the annealing time to 30 min leads to even more severe γ'-coarsening (Fig. 10). Reducing the annealing time to 10 min or even shorter exposes the 3D-printed superalloys to the risk of inhomogeneity in chemical composition. By balancing all these factors, we determined the heat treatment parameters to be 1270 °C for 15 min.

How much the non-uniform γ'-precipitates in the IRs would influence the high-temperature mechanical properties of the superalloy single crystal is of interest. To quantify the effects would require extensive future research but a rough estimate can be made here. It has been reported that the high temperature creep

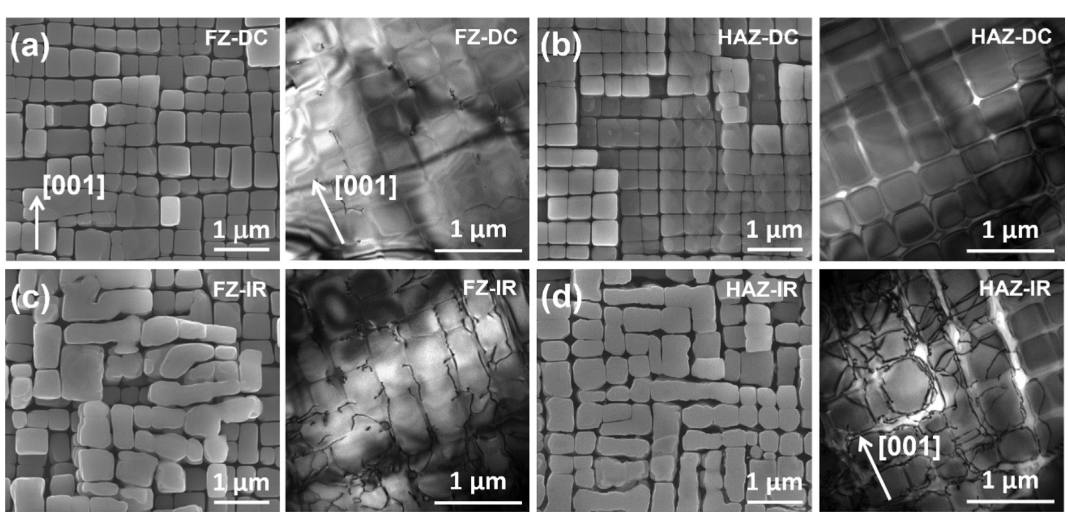

Fig. 10. The microstructure of laser-printed AM3 superalloy single crystal after being solutionizing annealed at 1270 °C for 30 min and then aged at 1100 °C and 870 °C for 6 h and 20 h, respectively. γ'-precipitates in the DCs of (a) FZ and (b) HAZ are uniform and dislocations are completely annihilated. Coarsening of γ'-precipitates in the IRs of (c) FZ and (d) HAZ occurs and dislocations tend to reside along the γ/γ' interface.

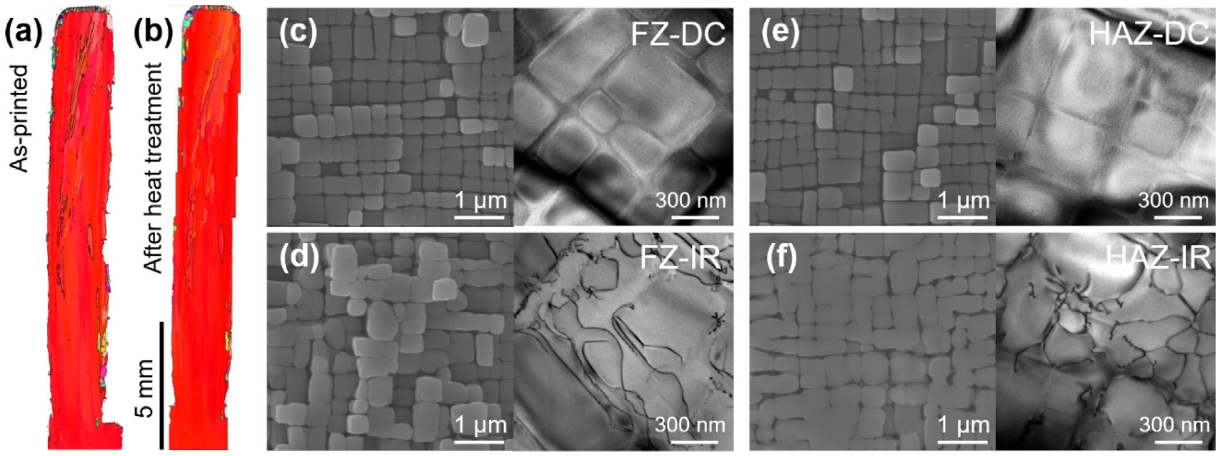

Fig. 11. The orientation and γ′-microstructure of the laser 3D-printed SRR99 super-alloy. (a-b) EBSD inverse pole figures indicate that after heat treatment, recrystallization is prevented, stray grain growth is suppressed, and thus the single crystal microstructure is kept. (c-f) SEM and TEM observations displaying that the γ′-precipitates have the same size and cuboidal morphology in the DCs of the fusion and heat affected zones, while γ′-particle coarsening is observed in the IRs.

properties of crept superalloy single crystal René 5 could be restored by 82 – 85 %, compared to the cast René 5 superalloy, by means of rejuvenation heat treatment with solutionizing at the temperature 28 °C below the solvus and then standard aging, while ~ 65 % of the high temperature creep properties could be restored when the solutionizing temperature is reduced to 56 °C below the solvus point [6]. It is inferred that elevating the solutionizing temperature is beneficial to the restoration of creep performance. In our study, the solutionizing temperature is only 10 °C below the solvus of the γ′-precipitates in IRs, so the creep performance is not expected to compromise much after the new heat treatment.

We note that the custom-designed annealing strategy to tackle the ***RASH*** issues reported in this study can be applicable to a variety of 3D-printed superalloys. Our heat treatment is successful for both laser and electron beam 3D-printed (or melted) AM3 superalloy single crystals. Laser 3D-printed SRR99 single crystal has also been tested (Fig. 11), with the same outcome when it comes to accomplishing ***RASH***.

Finally, the simplicity and efficiency are appealing attributes of our new custom-designed annealing approach. Compared to the previous "recovery annealing plus standard heat treatment", both time and energy consumption are markedly reduced, shortening the processing chain and reducing the associated costs and wasted parts. More importantly, the existing stray grains, which are unavoidable due to the nature of 3D printing, do not coarsen with this heat treatment. Since the service temperature of the single crystal blades will be lower than the solutionizing treatment temperature, we expect the stray grains to be stable during service. Our method also offers a double insurance in case there are occasionally some tiny stray grains leftover on the surface after post-printing machining or etching.

5. Conclusion

In summary, we have designed a new heat treatment protocol to release stored energy, avoid recrystallization, suppress stray grain growth, and homogenize the chemical and microstructure distribution, all of which are mandated for 3D-printing manufacture and repair of Ni-based superalloy single crystals. It is remarkable that the multiple ***RASH*** requirements are satisfied all at once, via an optimized solutionizing annealing treatment. Specifically, as ultra-fine dendrite width is generated by the steep temperature gradient of the 3D-printing process, the necessary distance for diffusion to cover is greatly reduced, making solutionizing heat treatment at the lower temperature adequate to accomplish chemical homogenization. Meanwhile, by setting the heat treatment temperature between the solvus points of DCs and IRs, the dislocations move freely in the DCs to annihilate fully, eliminating the stored energy that drives the nucleation of recrystallizing new grains, while the remaining precipitates in the IRs are able to hinder the motion and interactions of dislocations, the nucleation of recrystallization and the migration of stray grain boundaries. Meanwhile, our experiments and diffusion analysis successfully singled out an annealing time that is sufficiently long to homogenize the chemical species distribution, while as short as possible to limit the γ′-particle coarsening in the undissolved IRs. Via the construction of a temperature–time "treasure map", 1270 °C for 15 min is found to be the "sweet spot" for optimal solutionizing to resolve the ***RASH*** issues. Such a tactfully crafted heat treatment thus provides a much-needed stepping stone, for making 3D printing practical to the manufacture and repair of single-crystal superalloy parts, as exemplified above by the AM3 superalloy single crystals 3D-printed using either electron or laser beams, including those with leftover surface stray grains.

Author contributions.

K.C. designed the project in consultation with E.M. S.L. conducted the experiments and electron microscopy characterization. W.H. provided the additive-manufactured and re-melted specimens. S.L. analyzed and interpreted the µXRD data under the supervision of K.C. and N.T. K.C. and E.M. wrote the paper based on the draft from S.L. All authors contributed to the discussions of the results.

Data availability

The authors do not have permission to share data.

Declaration of Competing Interest

The authors declare that they have no known competing financial interests or personal relationships that could have appeared to influence the work reported in this paper.

Acknowledgements

This work is supported by the National Science and Technology Major Project (2019-VII-0019-0161), the National Natural Science

Foundation of China (Grant No. 51927801, U2032205), and 111 Project 2.0 (BP0618008). We thank Instrumental Analysis Center of Xi'an Jiaotong University for the assistance with EBSD analysis. We also appreciate the support from the International Joint Laboratory for Micro/Nano Manufacturing and Measurement Technologies. The ALS was supported by the Director, Office of Science, Office of Basic Energy Sciences, Materials Science Division, of the U.S. Department of Energy under Contract No. DE-AC02-05CH11231 at LBNL. E.M. acknowledges XJTU for supporting his work at CAID.

Appendix A. Supplementary material

Supplementary data to this article can be found online at https://doi.org/10.1016/j.matdes.2022.111075.

References:

[1] T.M. Pollock, Alloy design for aircraft engines, Nat. Mater. 15 (2016) 809, https://doi.org/10.1038/nmat4709.
[2] R.R. Srivastava, M.S. Kim, J.C. Lee, M.K. Jha, B.S. Kim, Resource recycling of superalloys and hydrometallurgical challenges, J. Mater. Sci. 49 (2014) 4671–4686, https://doi.org/10.1007/s10853-014-8219-y.
[3] P. Carter, D.C. Cox, C.A. Gandin, R.C. Reed, Process modelling of grain selection during the solidification of single crystal superalloy castings, Mater. Sci. Eng. A. 280 (2000) 233–246, https://doi.org/10.1016/S0921-5093(99)00701-7.
[4] T. DebRoy, T. Mukherjee, J.O. Milewski, J.W. Elmer, B. Ribic, J.J. Blecher, W. Zhang, Scientific, technological and economic issues in metal printing and their solutions, Nat. Mater. 18 (2019) 1026–1032, https://doi.org/10.1038/s41563-019-0408-2.
[5] C. Panwisawas, Y.T. Tang, R.C. Reed, Metal 3D printing as a disruptive technology for superalloys, Nat. Commun. 11 (2020) 2327, https://doi.org/10.1038/s41467-020-16188-7.
[6] L.H. Rettberg, P.G. Callahan, B.R. Goodlet, T.M. Pollock, Rejuvenation of Directionally Solidified and Single-Crystal Nickel-Base Superalloys, Metall. Mater. Trans. A Phys. Metall. Mater. Sci. 52 (2021) 1609–1631, https://doi.org/10.1007/s11661-021-06150-7.
[7] C. Körner, M. Ramsperger, C. Meid, D. Bürger, P. Wollgramm, M. Bartsch, G. Eggeler, Microstructure and Mechanical Properties of CMSX-4 Single Crystals Prepared by Additive Manufacturing, Metall. Mater. Trans. A Phys. Metall. Mater. Sci. 49 (2018) 3781–3792, https://doi.org/10.1007/s11661-018-4762-5.
[8] Y.J. Liang, X. Cheng, J. Li, H.M. Wang, Microstructural control during laser additive manufacturing of single-crystal nickel-base superalloys: New processing–microstructure maps involving powder feeding, Mater. Des. 130 (2017) 197–207, https://doi.org/10.1016/j.matdes.2017.05.066.
[9] A. Basak, R. Acharya, S. Das, Additive Manufacturing of Single-Crystal Superalloy CMSX-4 Through Scanning Laser Epitaxy: Computational Modeling, Experimental Process Development, and Process Parameter Optimization, Metall. Mater. Trans. A Phys. Metall. Mater. Sci. 47 (2016) 3845–3859, https://doi.org/10.1007/s11661-016-3571-y.
[10] K. Chen, R. Huang, Y. Li, S. Lin, W. Zhu, N. Tamura, J. Li, Z.W. Shan, E. Ma, Rafting-Enabled Recovery Avoids Recrystallization in 3D-Printing-Repaired Single-Crystal Superalloys, Adv. Mater. 32 (2020) 1907164, https://doi.org/10.1002/adma.201907164.
[11] D. Bürger, A.B. Parsa, M. Ramsperger, C. Körner, G. Eggeler, Creep properties of single crystal Ni-base superalloys (SX): A comparison between conventionally cast and additive manufactured CMSX-4 materials, Mater. Sci. Eng. A. 762 (2019), https://doi.org/10.1016/j.msea.2019.138098 138098.
[12] M. Ramsperger, L. Mújica Roncery, I. Lopez-Galilea, R.F. Singer, W. Theisen, C. Körner, Solution Heat Treatment of the Single Crystal Nickel-Base Superalloy CMSX-4 Fabricated by Selective Electron Beam Melting, Adv. Eng. Mater. 17 (2015) 1486–1493, https://doi.org/10.1002/adem.201500037.
[13] S.P. Murray, K.M. Pusch, A.T. Polonsky, C.J. Torbet, G.E. Seward, N. Zhou, S.A.J. Forsik, P. Nandwana, K.M. Michael, R.R. Dehoff, W. Slye, T.M. Pollock, A Defect-Resistant Co-Ni Superalloy for 3D Printing, Nat. Commun. 11 (2020) 4975, https://doi.org/10.1038/s41467-020-18775-0.
[14] I. Lopez-Galilea, B. Ruttert, J. He, T. Hammerschmidt, R. Drautz, B. Gault, W. Theisen, Additive manufacturing of CMSX-4 Ni-base superalloy by selective laser melting: Influence of processing parameters and heat treatment, Addit. Manuf. 30 (2019), https://doi.org/10.1016/j.addma.2019.100874 100874.
[15] B. Ruttert, M. Ramsperger, L. Mujica Roncery, I. Lopez-Galilea, C. Körner, W. Theisen, Impact of hot isostatic pressing on microstructures of CMSX-4 Ni-base superalloy fabricated by selective electron beam melting, Mater. Des. 110 (2016) 720–727, https://doi.org/10.1016/j.matdes.2016.08.041.
[16] R.C. Reed, C.M.F. Rae, Physical Metallurgy of the Nickel-based Superalloys, in: L. David E, K. Hono (Eds.), Physical Metallurgy, Elsevier, 2014, pp. 2215–2290.
[17] R.C. Reed, Superalloy fundamentals and applications, Cambridge University Press, Cambridge, UK, 2006.
[18] C. Körner, Additive manufacturing of metallic components by selective electron beam melting - A review, Int. Mater. Rev. 61 (2016) 361–377, https://doi.org/10.1080/09506608.2016.1176289.
[19] Y. Zhang, L. Wu, X. Guo, S. Kane, Y. Deng, Y.G. Jung, J.H. Lee, J. Zhang, Additive Manufacturing of Metallic Materials: A Review, J. Mater. Eng. Perform. 27 (2018) 1–13, https://doi.org/10.1007/s11665-017-2747-y.
[20] C.Y. Yap, C.K. Chua, Z.L. Dong, Z.H. Liu, D.Q. Zhang, L.E. Loh, S.L. Sing, Review of selective laser melting: Materials and applications, Appl. Phys. Rev. 2 (2015), https://doi.org/10.1063/1.4935926 041101.
[21] M. Gäumann, C. Bezençon, P. Canalis, W. Kurz, Single-crystal laser deposition of superalloys: Processing-microstructure maps, Acta Mater. 49 (2001) 1051–1062, https://doi.org/10.1016/S1359-6454(00)00367-0.
[22] G. Wang, J. Liang, Y. Yang, Y. Shi, Y. Zhou, T. Jin, X. Sun, Effects of scanning speed on microstructure in laser surface-melted single crystal superalloy and theoretical analysis, J. Mater. Sci. Technol. 34 (2018) 1315–1324, https://doi.org/10.1016/j.jmst.2017.11.027.
[23] R.M. Kearsey, J.C. Beddoes, P. Jones, P. Au, Compositional design considerations for microsegregation in single crystal superalloy systems, Intermetallics. 12 (2004) 903–910, https://doi.org/10.1016/j.intermet.2004.02.041.
[24] Y.J. Liang, H.M. Wang, Origin of stray-grain formation and epitaxy loss at substrate during laser surface remelting of single-crystal nickel-base superalloys, Mater. Des. 102 (2016) 297–302, https://doi.org/10.1016/j.matdes.2016.04.051.
[25] T.D. Anderson, J.N. DuPont, T. DebRoy, Origin of stray grain formation in single-crystal superalloy weld pools from heat transfer and fluid flow modeling, Acta Mater. 58 (2010) 1441–1454, https://doi.org/10.1016/j.actamat.2009.10.051.
[26] R. Bürgel, P.D. Portella, J. Preuhs, Recrystallization in single crystal of nickel base superalloy, in: T.M. Pollock, R.D. Kissinger (Eds.), Superalloys 2000, TMS, Warrendale, PA, USA, 2000, pp. 229–238.
[27] J. Kuipers, K. Wiens, B. Ruggiero, Rejuvenation heat treatment of single crystal gas turbine blades, in: Proc. ASME Turbo Expo 2017, ASME, Charlotte, NC, USA, 2017: pp. GT2017–63698. https://doi.org/10.1115/GT2017-63698.
[28] G.E. Fuchs, B.A. Boutwell, Modeling of the partitioning and phase transformation temperatures of an as-cast third generation single crystal Ni-base superalloy, Mater. Sci. Eng. A. 333 (2002) 72–79, https://doi.org/10.1016/S0921-5093(01)01825-1.
[29] K.Y. Cheng, C.Y. Jo, T. Jin, Z.Q. Hu, Influence of applied stress on the γ' directional coarsening in a single crystal superalloy, Mater. Des. 31 (2010) 968–971, https://doi.org/10.1016/j.matdes.2009.08.018.
[30] R.C. Reed, D.C. Cox, C.M.F. Rae, Kinetics of rafting in a single crystal superalloy: Effects of residual microsegregation, Mater. Sci. Technol. 23 (2007) 893–902, https://doi.org/10.1179/174328407X192723.
[31] U. Brückner, A. Epishin, T. Link, K. Dressel, The influence of the dendritic structure on the γ/γ'-lattice misfit in the single-crystal nickel-base superalloy CMSX-4, Mater. Sci. Eng. A. 247 (1998) 23–31, https://doi.org/10.1016/s0921-5093(97)00856-3.
[32] X. Milhet, M. Arnoux, J. Cormier, J. Mendez, C. Tromas, On the influence of the dendritic structure on the creep behavior of a Re-containing superalloy at high temperature/low stress, Mater. Sci. Eng. A. 546 (2012) 139–145, https://doi.org/10.1016/j.msea.2012.03.041.
[33] S. Gorsse, C. Hutchinson, M. Gouné, R. Banerjee, Additive manufacturing of metals: a brief review of the characteristic microstructures and properties of steels, Ti-6Al-4V and high-entropy alloys, Sci. Technol. Adv. Mater. 18 (2017) 584–610, https://doi.org/10.1080/14686996.2017.1361305.
[34] E. Chauvet, P. Kontis, E.A. Jägle, B. Gault, D. Raabe, C. Tassin, J.J. Blandin, R. Dendievel, B. Vayre, S. Abed, G. Martin, Hot cracking mechanism affecting a non-weldable Ni-based superalloy produced by selective electron Beam Melting, Acta Mater. 142 (2018) 82–94, https://doi.org/10.1016/j.actamat.2017.09.047.
[35] C. Ren, L. Jiang, J. Kou, S. Yan, L. Li, M. Liu, X. Dong, K. Chen, Z. Li, Z. Li, X. Huang, R. Tai, Development of micro-Laue technique at Shanghai Synchrotron Radiation Facility for materials sciences, Sci. China Mater. 64 (9) (2021) 2348–2358, https://doi.org/10.1007/s40843-021-1648-3.
[36] O.M. Horst, B. Ruttert, D. Bürger, L. Heep, H. Wang, A. Dlouhý, W. Theisen, G. Eggeler, On the rejuvenation of crept Ni-Base single crystal superalloys (SX)by hot isostatic pressing (HIP), Mater. Sci. Eng. A. 758 (2019) 202–214, https://doi.org/10.1016/j.msea.2019.04.078.
[37] J. Yu, X. Sun, N. Zhao, T. Jin, H. Guan, Z. Hu, Effect of heat treatment on microstructure and stress rupture life of DD32 single crystal Ni-base superalloy, Mater. Sci. Eng. A. 460–461 (2007) 420–427, https://doi.org/10.1016/j.msea.2007.01.117.
[38] S. Ci, J. Liang, J. Li, Y. Zhou, X. Sun, Microstructure and tensile properties of DD32 single crystal Ni-base superalloy repaired by laser metal forming, J. Mater. Sci. Technol. 45 (2020) 23–34, https://doi.org/10.1016/j.jmst.2020.01.003.
[39] S. Steuer, Z. Hervier, S. Thabart, C. Castaing, T.M. Pollock, J. Cormier, Creep behavior under isothermal and non-isothermal conditions of AM3 single crystal superalloy for different solutioning cooling rates, Mater. Sci. Eng. A. 601 (2014) 145–152, https://doi.org/10.1016/j.msea.2014.02.046.
[40] M. Kunz, N. Tamura, K. Chen, A.A. MacDowell, R.S. Celestre, M.M. Church, S. Fakra, E.E. Domning, J.M. Glossinger, J.L. Kirschman, G.Y. Morrison, D.W. Plate, B.V. Smith, T. Warwick, V.V. Yashchuk, H.A. Padmore, E. Ustundag, A dedicated superbend x-ray microdiffraction beamline for materials, geo-, and environmental sciences at the advanced light source, Rev. Sci. Instrum. 80 (2009) 035108.

[41] J. Kou, K. Chen, N. Tamura, A peak position comparison method for high-speed quantitative Laue microdiffraction data processing, Scr. Mater. 143 (2018) 49–53, https://doi.org/10.1016/j.scriptamat.2017.09.005.
[42] G. Zhou, W. Pantleon, R. Xu, W. Liu, K. Chen, Y. Zhang, Quantification of local dislocation density using 3D synchrotron monochromatic X-ray microdiffraction, Mater. Res. Lett. 9 (2021) 183–189, https://doi.org/10.1080/21663831.2020.1862932.
[43] Y. Li, K. Chen, X. Dang, F. Zhang, N. Tamura, C.S. Ku, H. Kang, H.R. Wenk, XtalCAMP: A comprehensive program for the analysis and visualization of scanning Laue X-ray micro-/nanodiffraction data, J. Appl. Crystallogr. 53 (2020) 1392–1403, https://doi.org/10.1107/S1600576720010882.
[44] S.R. Hegde, R.M. Kearsey, J.C. Beddoes, Designing homogenization-solution heat treatments for single crystal superalloys, Mater. Sci. Eng. A. 527 (2010) 5528–5538, https://doi.org/10.1016/j.msea.2010.05.019.
[45] Y. Li, K. Chen, R.L. Narayan, U. Ramamurty, Y. Wang, J. Long, N. Tamura, X. Zhou, Multi-scale microstructural investigation of a laser 3D printed Ni-based superalloy, Addit. Manuf. 34 (2020), https://doi.org/10.1016/j.addma.2020.101220 101220.
[46] D.M. Norfleet, D.M. Dimiduk, S.J. Polasik, M.D. Uchic, M.J. Mills, Dislocation structures and their relationship to strength in deformed nickel microcrystals, Acta Mater. 56 (2008) 2988–3001, https://doi.org/10.1016/j.actamat.2008.02.046.
[47] O.M. Barabash, J.A. Horton, S.S. Babu, J.M. Vitek, S.A. David, J.W. Park, G.E. Ice, R. I. Barabash, Evolution of dislocation structure in the heat affected zone of a nickel-based single crystal, J. Appl. Phys. 96 (2004) 3673–3679, https://doi.org/10.1063/1.1777393.
[48] M.S.A. Karunaratne, D.C. Cox, P. Carter, R.C. Reed, Modelling of the Microsegregation in CMSX-4 Superalloy and its Homogenisation During Heat Treatment, in: T.M. Pollock, R.D. Kissinger (Eds.), Superalloys 2000, TMS, Warrendale, PA, USA, 2000, pp. 263–272.
[49] J.A.S.B. Cardoso, A. Almeida, R. Vilar, Microstructure of a coated single crystalline René N5 part repaired by epitaxial laser deposition, Addit. Manuf. 49 (2022), https://doi.org/10.1016/j.addma.2021.102515 102515.
[50] X. Su, Q. Xu, R. Wang, Z. Xu, S. Liu, B. Liu, Microstructural evolution and compositional homogenization of a low Re-bearing Ni-based single crystal superalloy during through progression of heat treatment, Mater. Des. 141 (2018) 296–322, https://doi.org/10.1016/j.matdes.2017.12.020.
[51] P. Kontis, Z. Li, D.M. Collins, J. Cormier, D. Raabe, B. Gault, The effect of chromium and cobalt segregation at dislocations on nickel-based superalloys, Scr. Mater. 145 (2018) 76–80, https://doi.org/10.1016/j.scriptamat.2017.10.005.